Complete Unitary Qutrit Control in Ultracold Atoms

Joseph Lindon⬤, Arina Tashchilina, Logan W. Cooke⬤, and Lindsay J. LeBlanc⬤*

Department of Physics, University of Alberta, Edmonton, Alberta, Canada

Physical quantum systems are commonly composed of more than two levels and offer the capacity to encode information in higher-dimensional spaces beyond the qubit, starting with the three-level qutrit. Here, we encode neutral-atom qutrits in an ensemble of ultracold ^{87}Rb and demonstrate arbitrary single-qutrit SU(3) gates. We generate a full set of gates using only two resonant microwave tones, including synthesizing a gate that effects a direct coupling between the two disconnected levels in the three-level Λ-scheme. Using two different gate sets, we implement and characterize the Walsh-Hadamard Fourier transform, and find similar final-state fidelity and purity from both approaches. This work establishes the ultracold neutral-atom qutrit as a promising platform for qutrit-based quantum information processing, extensions to d-dimensional qudits, and explorations in multilevel quantum state manipulations with nontrivial geometric phases.

DOI: 10.1103/PhysRevApplied.19.034089

I. INTRODUCTION

The conventional paradigm for universal quantum computing makes use of two-level qubits, but higher-dimensional quantum systems offer considerable advantages. Logical operations and information storage using three-level systems ("qutrits") in a larger Hilbert space give way to algorithms that can be more efficient [1] and allow for more complex entanglement than qubits [2]. Qutrits [3] and higher d-dimensional qudits [4] are valuable as a quantum resources for speed-up and for improved cryptographic security in transmission over quantum networks [5–7]. Additionally, using a third temporary-state level during the implementation of a qubit gate can significantly improve fidelities and reduce circuit complexity [7–10].

While qubits are readily simulated by the polarization of classical light, qutrits offer an additional complexity that reflects their inherently quantum properties [3]. Many physical platforms have served as host to qutrits [1,11,12], including photonic systems [6,13–18], NMR ensembles [3], superconducting quantum circuits [19–24], and trapped ions [11,25–28]. In contrast to qubit operations, single *qutrit* gates are represented by 3×3 unitary matrices in the group SU(3), generated by the eight Gell-Mann matrices $\hat{\lambda}_i$ [2]. Experimental qutrit demonstrations to date have realized arbitrary operations by decomposing the desired transformation into three SU(2) operations followed by a diagonal phase gate [11,21,22,29]. In many

physical systems, two of the three SU(2) couplings are accessible, but selection rules dictated by parity mean that the third is less convenient or even forbidden. To overcome this, two resonant couplings on the accessible transitions can be combined as a simultaneous dual-tone operator to synthesize the third coupling [11].

In this work, we demonstrate and manipulate neutral-atom qutrits in ultracold ensembles, taking advantage of the well-defined, long-lived, and readily controlled hyperfine transitions in the alkali metals. We synthesize arbitrary single-qutrit gates using two different schemes, both of which require only two couplings in the three-state manifold (Fig. 1). In one of these approaches [11], we show an effective coupling between two levels that are not simply connected by microwave fields, establishing a comprehensive set of two-state operations within the three-state manifold. In contrast to atomic experiments demonstrating multilevel state control across the entire hyperfine manifold [30,31], we specifically isolate and address three (and only three) levels among the eight available to engineer our qutrit. Ensemble systems like ours provide a testbed for general quantum information processing with neutral-atom arrays [32–35]. Adapting the ensemble approach described here to address individual atoms could be achieved through site-specific gradients, focused light shifts, or phase control [36–39], opening up the advantages of qutrits across atomic quantum computing platforms. More broadly, the approach to quantum state control demonstrated here will provide tools for exploring fundamental operations on multilevel systems, including engineering nontrivial geometric phases in atomic systems [40–42].

———————
*Author to whom correspondence should be addressed: lindsay.leblanc@ualberta.ca
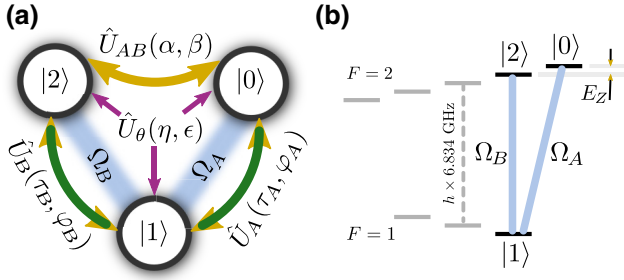
(a)

(b)

FIG. 1. (a) Schematic representation the three qutrit levels $\{|0\rangle, |1\rangle, |2\rangle\}$, where direct couplings (Ω_A and Ω_B) exist only between $|0\rangle \leftrightarrow |1\rangle$ and $|1\rangle \leftrightarrow |2\rangle$, and are associated with unitary operations $\hat{U}_A$ and $\hat{U}_B$. With a dual-tone operator, coupling between $|0\rangle \leftrightarrow |2\rangle$ is possible via $\hat{U}_{AB}$; an additional phase-only operator $\hat{U}_\theta$ can be applied across all levels. (b) Energy-level diagram of the ^{87}Rb ground-state manifold, with levels $|0\rangle \rightarrow |F = 2, m_F = 2\rangle$, $|1\rangle \rightarrow |F = 1, m_F = 1\rangle$, and $|2\rangle \rightarrow |F = 2, m_F = 1\rangle$ connected by two magnetic dipole transitions at microwave frequencies, whose energy difference is controlled by the Zeeman splitting, E_Z.

II. SINGLE-QUTRIT GATES

A qutrit $|\psi\rangle = \sum_{k=0}^{2} c_k e^{i\phi_k} |k\rangle$ is defined by the parameters $\{c_k\}$ and $\{\phi_k\}$, four of which are independent after considering normalization and global phase invariance. A single-qutrit gate, part of SU(3), is defined by eight independent parameters [29]. In a system with only two (complex) couplings [Fig. 1(a)], sequential operations can be applied to span all eight parameters, followed by a two-parameter relative phase adjustment, $\hat{U}_\theta(\eta, \epsilon)$. In one approach [3,22,24], a general single-qutrit gate is implemented with single-tone operators, such as

$$\hat{U}_{\text{gen.}}^{\text{I}} = \hat{U}_\theta(\eta, \epsilon) \hat{U}_B(\tau_{B2}, \varphi_{B2}) \hat{U}_A(\tau_{A1}, \varphi_{A1}) \hat{U}_B(\tau_{B1}, \varphi_{B1}),$$

where $\tau_{Xi} = |\Omega_X| t / 2$ and $\varphi_{Xi} = \arg(\Omega_X)$ are the pulse areas and coupling phases for transitions $X = \{A, B\}$ with parameter index i, and $\{\eta, \epsilon\}$ are relative phase adjustments (Appendix A 2).

In a second approach [11], a dual-tone operator is used to simultaneously drive both transitions A and B to synthesize a third direct coupling $\hat{U}_{AB}(\alpha, \beta)$ between states $|0\rangle \leftrightarrow |2\rangle$, where the operator duration is exactly $t_{AB} = 2\pi / \sqrt{|\Omega_A|^2 + |\Omega_B|^2}$ and the parameters α and β are derived from the complex couplings $\Omega_{A,B}$ (see Appendix A 1). A general gate is implemented through a combination of operators such as

$$\hat{U}_{\text{gen.}}^{\text{II}} = \hat{U}_\theta(\eta, \epsilon) \hat{U}_B(\tau_{B2}, \varphi_{B2}) \hat{U}_A(\tau_{A1}, \varphi_{A1}) \hat{U}_{AB}(\alpha, \beta).$$

In both decompositions I and II, the first SU(2) operator $\hat{U}_{AB,B}$ is designed such that $\hat{U}_{\text{gen.}} \hat{U}_{AB,B}^\dagger$ has one off-diagonal matrix element of zero. The second pulse $\hat{U}_A$ zeroes three

more off-diagonal matrix elements in $\hat{U}_{\text{gen.}} \hat{U}_{AB,B}^\dagger \hat{U}_A^\dagger$, and after the third only a diagonal phase remains which is implemented by $\hat{U}_\theta$ (see Appendix A 3).

As a particular example of a single-qutrit gate that uses control over all eight parameters, we consider the Walsh-Hadamard gate, which is the single-qutrit Fourier transform [11],

$$\hat{F} = \frac{1}{\sqrt{3}} \begin{pmatrix} 1 & 1 & 1 \\ 1 & e^{2\pi i/3} & e^{-2\pi i/3} \\ 1 & e^{-2\pi i/3} & e^{i2\pi/3} \end{pmatrix}. \quad (1)$$

This transform has broad applications, such as Shor's algorithm [29], error correction [21], implementing the SWAP gate, and the Bernstein-Vazirani algorithm [1]. In the single- and dual-tone operator decompositions described above, the Fourier transforms are implemented as

$$\hat{F}^{\text{I}} = e^{i\pi/6} \hat{U}_\theta\left(-\frac{\pi}{6}, -\frac{\pi}{6}\right) \hat{U}_B\left(\frac{5\pi}{4}, \frac{\pi}{2}\right) \hat{U}_A\left(\tau_A^{\text{I}}, \pi\right)$$
$$\cdot \hat{U}_B\left(\frac{\pi}{4}, 0\right),$$
$$\hat{F}^{\text{II}} = i\hat{U}_\theta\left(\frac{\pi}{3}, -\frac{\pi}{2}\right) \hat{U}_A\left(\frac{\pi}{4}, \frac{\pi}{6}\right) \hat{U}_B\left(\tau_B^{\text{II}}, \frac{\pi}{3}\right)$$
$$\cdot \hat{U}_{AB}\left(\frac{\pi}{4}, -\frac{2\pi}{3}\right),$$

where $\tau_A^{\text{I}} = \arccos(-1/3)/2$ and $\tau_B^{\text{II}} = \pi + \arctan(1/\sqrt{2})$.

We implement both the single- and dual-tone Fourier transform operators to experimentally explore ultracold atomic ensembles as a platform for qutrit operations, and to compare the two approaches to qutrit operators in terms of final-state fidelity and purity.

III. EXPERIMENTAL METHODS

In our experiments, we prepare ultracold ensembles of ^{87}Rb atoms, manipulate the internal electronic states [Fig. 1(b)] using resonant microwave pulses, and measure the results by analyzing the final state via absorption imaging. The ensemble approach allows us to perform simultaneous experiments on a large number (around 10^5) of identical atoms using spatially uniform fields, and the measurement over the entire ensemble gives a statistical measure of the final state in a single experimental run.

In particular, we prepare 10^5 Bose-Einstein condensed ^{87}Rb atoms in an optical dipole trap. The ground $5^2 S_{1/2}$ state of ^{87}Rb has two hyperfine levels, $F = 1$ and $F = 2$, separated by $\omega_0 = 2\pi \times 6.835$ GHz, each of which hosts $2F + 1$ Zeeman sublevels, which are energetically split by $E_Z \approx h \times 1.7$ MHz in a weak magnetic field. Using optical pumping, we initialize all atoms in the spin-polarized input state $|\psi_{\text{in}}\rangle = |0\rangle \equiv |F = 2, m_F = 2\rangle$. Optionally, we then use π-pulse operations ($\hat{U}_A$ or $\hat{U}_B \hat{U}_A$ pulses) to prepare

initial states $|\psi_{in}\rangle = |1\rangle$ or $|2\rangle$. In this work, we use only microwave couplings between states of different F to complete operations, avoiding the radio-frequency couplings between levels in the same F manifold, which would allow direct $|0\rangle$ to $|2\rangle$ coupling. By doing this, we avoid simultaneous couplings between all m_F states in that manifold, due to the degeneracy of the Zeeman transitions in a weak magnetic field. The microwave transitions we use are, in contrast, nondegenerate, even in weak magnetic fields.

Amplitude- and phase-controlled microwave signals, tuned near ω_0, are resonant with the "A" $|0\rangle \leftrightarrow |1\rangle \equiv |F = 1, m_F = 1\rangle$ and "B" $|1\rangle \leftrightarrow |2\rangle \equiv |F = 2, m_F = 1\rangle$ transitions with typical Rabi frequencies $|\Omega_{A,B}| \sim 2\pi \times 2$ kHz. These two microwave tones, timed appropriately, effect the unitary operations $\hat{U}_A$ or $\hat{U}_B$ when used alone, and $\hat{U}_{AB}$ when driven together (Appendix A 1). Figures 2(d) and 2(e) show two examples of the dual-tone operator $\hat{U}_{AB}$ acting on initial state $|\psi_{in}\rangle = |0\rangle$ for varying pulse times: at the operator time t_{AB}, the results show the populations distributed between $|0\rangle$ and $|2\rangle$ only. This distribution is controlled by the parameters α and β, which themselves depend on the amplitudes and phases of Ω_A and Ω_B; with this technique we can create any superposition between $|0\rangle$ and $|2\rangle$.

To effect a general single-qutrit gate, up to three of these operators are applied to the system, along with relative phase control (Appendix A 4). To decipher the amplitude and phase information of the resulting output-state qutrits $|\psi_{out}\rangle$, we perform tomography by applying rotation operations to the system (see below for details). After the operations are complete, the atoms are released from the trap and the populations $|c_i|^2$ of each level in the qutrit are measured via absorption imaging: the three levels are spatially separated by a Stern-Gerlach magnetic field gradient in time of flight, and counted simultaneously in a single absorption image [Fig. 2(b)].

IV. TOMOGRAPHY

To determine the full effect of the single-qutrit gates, we perform quantum state tomography on the final states $|\psi_{out}\rangle$ for each of $\hat{U}^{I}_{gen.}$ and $\hat{U}^{II}_{gen.}$ acting on three orthogonal input states, $|\psi_{in}\rangle = \{|0\rangle, |1\rangle, |2\rangle\}$. Eight linearly independent projections of the qutrit state are required to fully characterize its density matrix $\hat{\rho} = \hat{\mathbb{1}}/3 + (1/3)\sum_{k=1}^{8}\langle\hat{\lambda}_k\rangle\hat{\lambda}_k$ [2].

To perform the tomography, readout operators $\hat{R}_i$ (Table I) are applied before projective measurement. Table II shows how the orthogonal Gell-Mann matrices can be constructed from these projections. The usual projection operation $\langle\psi_{out}|\chi\rangle\langle\chi|\psi_{out}\rangle$ extends to $\text{tr}(|\chi\rangle\langle\chi|\hat{\rho}_{out})$ when a density matrix $\hat{\rho}_{out}$ is substituted for the pure state $|\psi_{out}\rangle$. We measure three projections for each
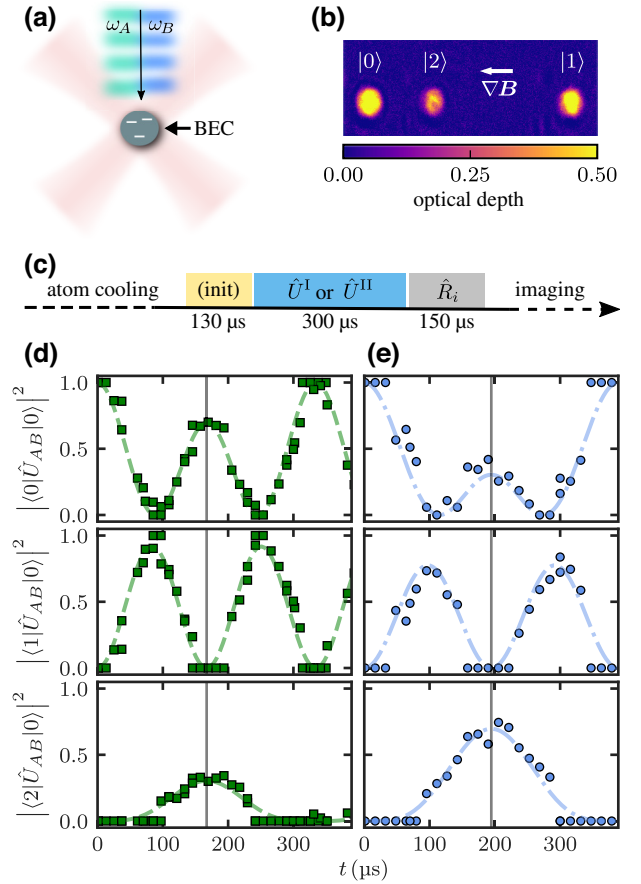

FIG. 2.   (a) A Bose-Einstein condensate of ^{87}Rb is trapped at the intersection of two optical dipole beams. Resonant microwave radiation with frequencies ω_A and/or ω_B drives transitions between levels. (b) A magnetic field gradient $\nabla\mathbf{B}$ is applied to the atoms during time of flight, before absorption imaging, spatially separating atomic levels according to their magnetic moments, μ_i, where $\mu(|0\rangle) = \mu_B$, $\mu(|1\rangle) = -\mu_B/2$, and $\mu(|2\rangle) = \mu_B/2$, and μ_B is the Bohr magneton. The color map represents an absorption image after 25 ms time of flight, with color bar indicating the optical depth of the atoms in clouds associated with each level. (c) Timing sequence for cooling, state initialization, qutrit gates $\hat{U}^{I,II}$, and tomography rotations $\hat{R}_i$. (d),(e) Example calibration data for dual-tone operators $\hat{U}_{AB}(0.19\pi, 0)$ in (d) and $\hat{U}_{AB}(0.31\pi, 0)$ in (e). Vertical gray lines indicate the operator time t_{AB} for which the intermediate-state $|1\rangle$ population/amplitude is zero. The dashed and dash-dotted curves in (d),(e) are the population dynamics simulations of the coupled three-level system, using the α and β parameters indicated above.

of the six readout operators, $\langle\hat{R}_i^{\dagger}|0\rangle\langle0|\hat{R}_i\rangle$, $\langle\hat{R}_i^{\dagger}|1\rangle\langle1|\hat{R}_i\rangle$, and $\langle\hat{R}_i^{\dagger}|2\rangle\langle2|\hat{R}_i\rangle$, and in total, we measure 6×3 projections, which are not all linearly independent.

An iterative maximum likelihood technique [43] allows us to estimate the density matrix $\hat{\rho}$ while maintaining the

TABLE I. Readout operators used for quantum state tomography. They are all $\pi/2$-area pulses.

$\hat{R}_i$	Basis	Phase ϕ	Matrix form
$\hat{R}_1$	$\{|0\rangle, |1\rangle\}$	0	$\frac{1}{\sqrt{2}}\begin{pmatrix} 1 & -1 & 0 \\ 1 & 1 & 0 \\ 0 & 0 & \sqrt{2} \end{pmatrix}$
$\hat{R}_2$	$\{|0\rangle, |1\rangle\}$	$\frac{\pi}{2}$	$\frac{1}{\sqrt{2}}\begin{pmatrix} 1 & -i & 0 \\ -i & 1 & 0 \\ 0 & 0 & \sqrt{2} \end{pmatrix}$
$\hat{R}_3$	$\{|1\rangle, |2\rangle\}$	0	$\frac{1}{\sqrt{2}}\begin{pmatrix} \sqrt{2} & 0 & 0 \\ 0 & 1 & 1 \\ 0 & -1 & 1 \end{pmatrix}$
$\hat{R}_4$	$\{|1\rangle, |2\rangle\}$	$\frac{\pi}{2}$	$\frac{1}{\sqrt{2}}\begin{pmatrix} \sqrt{2} & 0 & 0 \\ 0 & 1 & -i \\ 0 & -i & 1 \end{pmatrix}$
$\hat{R}_5$	$\{|0\rangle, |2\rangle\}$	0	$\frac{1}{\sqrt{2}}\begin{pmatrix} 1 & 0 & -1 \\ 0 & -\sqrt{2} & 0 \\ -1 & 0 & -1 \end{pmatrix}$
$\hat{R}_6$	$\{|0\rangle, |2\rangle\}$	$\frac{\pi}{2}$	$\frac{1}{\sqrt{2}}\begin{pmatrix} 1 & 0 & -i \\ 0 & -\sqrt{2} & 0 \\ i & 0 & -1 \end{pmatrix}$

condition $\text{tr}(\hat{\rho}) = 1$. Using the function

$$\hat{Q}(\hat{\rho}) = \sum_i \sum_{j=0,1,2} \frac{f_j^{\ i}}{\text{tr}\left(\hat{R}_i^\dagger |j\rangle\langle j|\hat{R}_i\hat{\rho}\right)}\hat{R}_i^\dagger |j\rangle\langle j|\hat{R}_i, \quad (2)$$

where $f_j^{\ i}$ is the cloud fraction found experimentally in eigenstate $|j\rangle$ after the readout operator $\hat{R}_i$ is applied, we iterate through

$$\hat{\rho}_{i+1} = \frac{\hat{Q}(\hat{\rho}_i)\hat{\rho}_i\hat{Q}(\hat{\rho}_i)}{\text{tr}\left(\hat{Q}(\hat{\rho}_i)\hat{\rho}_i\hat{Q}(\hat{\rho}_i)\right)} \quad (3)$$

TABLE II. Demonstration of the Gell-Mann matrices constructed using readout operators $\hat{R}_i$.

$\hat{\lambda}_i$	Construction
$\hat{\lambda}_1$	$\hat{R}_1^\dagger (|1\rangle\langle 1| - |0\rangle\langle 0|)\hat{R}_1$
$\hat{\lambda}_2$	$\hat{R}_2^\dagger (|0\rangle\langle 0| - |1\rangle\langle 1|)\hat{R}_2$
$\hat{\lambda}_3$	$\hat{R}_3^\dagger |2\rangle\langle 2|\hat{R}_3 - \hat{R}_5^\dagger |1\rangle\langle 1|\hat{R}_5$[a]
$\hat{\lambda}_4$	$\hat{R}_5^\dagger (|2\rangle\langle 2| - |0\rangle\langle 0|)\hat{R}_5$
$\hat{\lambda}_5$	$\hat{R}_6^\dagger (|0\rangle\langle 0| - |2\rangle\langle 2|)\hat{R}_6$
$\hat{\lambda}_6$	$\hat{R}_3^\dagger (|1\rangle\langle 1| - |2\rangle\langle 2|)\hat{R}_3$
$\hat{\lambda}_7$	$\hat{R}_4^\dagger (|1\rangle\langle 1| - |2\rangle\langle 2|)\hat{R}_4$
$\hat{\lambda}_8$	$\left(\hat{R}_3^\dagger |0\rangle\langle 0|\hat{R}_3 + \hat{R}_5^\dagger |1\rangle\langle 1|\hat{R}_5 - 2\hat{R}_1^\dagger |2\rangle\langle 2|\hat{R}_1\right)/\sqrt{3}$[b]

[a] One of four possibilities shown
[b] One of eight possibilities shown

until convergence, having begun with the maximally mixed density matrix $\hat{\rho}_0 = \hat{\mathbb{1}}/3$ (Ref. [2]).

V. RESULTS

We applied the Walsh-Hadamard decompositions $\hat{F}^{\text{I}}$ and $\hat{F}^{\text{II}}$ on three input computational basis states, $|0\rangle$, $|1\rangle$, and $|2\rangle$, and characterize the output state's density matrix, $\hat{\rho}_{\text{out}}$. Figure 3 shows one such density-matrix reconstruction, after applying $\hat{F}^{\text{II}}$ to the state $|0\rangle$. For each tomographically measured $\hat{\rho}_{\text{out}}$ (resulting from one of $\hat{F}^{\text{I,II}}$ acting on an input basis state $|n\rangle$), we calculate the quantum state fidelity [44]

$$\mathcal{F}(\hat{F}, |n\rangle) = \langle n|\hat{F}^\dagger \hat{\rho}_{\text{out}}\hat{F}|n\rangle \quad (4)$$

and purity $\mathcal{P}(\hat{\rho}_{\text{out}}) = \text{tr}(\hat{\rho}_{\text{out}}^2)$. Table III shows that the single-qutrit gates operate as expected for all input basis states, and that the two decompositions produce states with similar fidelities and purities.

The ensemble approach taken in this work gives excellent statistics and provides a fast path towards calibrating the pulse areas and phases. However, this approach is not without its limitations, which we see in the values for both the fidelity $\mathcal{F}$ and purity $\mathcal{P}$. After averaging each measurement over $N \geq 10$ experimental trials (Fig. 4), we find that variations in the results decrease with increasing N, but the average values remain similar to the single $N = 1$ trial. This indicates that shot-to-shot noise is not a significant
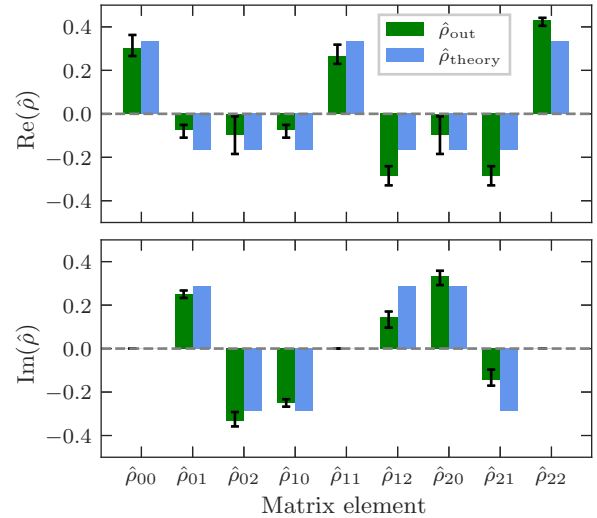

FIG. 3. Reconstructed density matrix elements from the measured values $\hat{\rho}_{\text{out}}$ (green, left bars) and for the modeled, expected density matrix $\hat{\rho}_{\text{theory}}$ (blue, right bars) for the dual-tone Walsh-Hadamard (Fourier) operator acting on the initial state $|0\rangle$: $\hat{F}^{\text{II}}|0\rangle$. The real (upper) $\text{Re}(\hat{\rho})$ and imaginary (lower) $\text{Im}(\hat{\rho})$ parts of these elements are shown. Error bars show the range of each matrix element across all $N = 10$ tomographic measurements. As a Hermitian operator, the main diagonal of $\hat{\rho}$ is real.

TABLE III. Fidelity and purity found by maximum likelihood estimation after state tomography for two decompositions of the single-qutrit Fourier transform. Errors shown are the standard deviation of values across the N tomographic measurements. State preparation and measurement errors are not removed.

Operator	$|\psi_{\text{in}}\rangle$	N	$\mathcal{P}$	$\mathcal{F}$	$\mathcal{F}_{\text{pure}}$
$\hat{F}^{\text{II}}$	$|0\rangle$	10	0.93(4)	0.91(2)	0.95(2)
	$|1\rangle$	10	0.92(3)	0.91(2)	0.96(2)
	$|2\rangle$	10	0.90(6)	0.86(4)	0.92(2)
$\hat{F}^{\text{I}}$	$|0\rangle$	15	0.90(8)	0.92(6)	0.98(3)
	$|1\rangle$	12	0.88(8)	0.87(5)	0.95(3)
	$|2\rangle$	16	0.89(4)	0.89(7)	0.95(7)

contributor to the infidelity and impurity of these measures. In contrast, we find that the impurity of the final states impacts the fidelity: if we assume the nearest pure state is achieved before calculating the fidelity using Eq. (4) by estimating that state as

$$\hat{\rho} \to \frac{\hat{\rho} - \hat{\mathbb{1}}/3}{\mathcal{P}(\hat{\rho})} + \frac{\hat{\mathbb{1}}}{3}, \tag{5}$$

we find better $\mathcal{F}_{\text{pure}}$ than $\mathcal{F}$, indicating that a significant part of the infidelity arises from loss of purity. Spatial inhomogeneities in the coupling fields or the environment experienced by atoms may cause position-dependent evolution and appear as a loss of ensemble purity. Our analysis
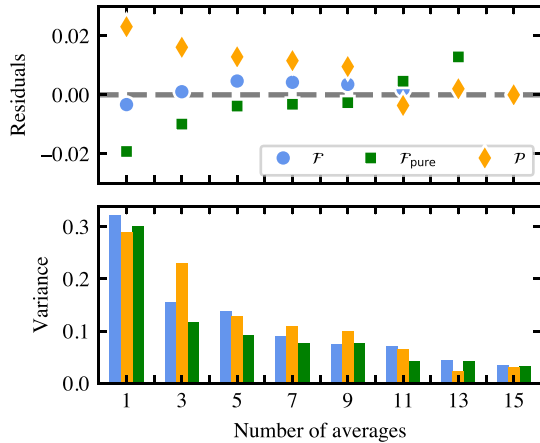

FIG. 4. Gate-quality metrics $\mathcal{F}$, $\mathcal{P}$, and $\mathcal{F}_{\text{pure}}$ after averaging over N of the sequences from Table III. The upper plot shows the residuals for results with respect to the average over $N = 15$ scans, and the lower plot shows the variance of the results (given as the variance between the maximum and the minimum of each metric): left blue bars, $\mathcal{F}$; middle yellow bars, $\mathcal{P}$; right green bars, $\mathcal{F}_{\text{pure}}$. While the variance reduces with more averaging, as expected, there is minimal change in the average value (seen via the residuals), suggesting that random errors from one experiment to the next are not a dominant error mechanism.

(Appendix B 4) suggests the dominant effect is dephasing of the qutrit due to Stark-shift inhomogeneity in the optical dipole trap: atoms in the center of the trap have a detuning of the order of 400 Hz relative to those at the edges, and because the atoms are cold and move little during the operation time, this difference does not average out over the course of a gate sequence. Improvements could be made by moving the measurements to time of flight (Appendix B 4), and faster operations may be possible (at the expense of some spontaneous emission) using two-photon optical transitions [45,46]. A probable source of the remaining infidelity is imprecision in the calibration of individual operators.

VI. DISCUSSION

We successfully demonstrated arbitrary SU(3) control in neutral alkali atoms using the Walsh-Hadamard (Fourier transform) single-qutrit gate, while implementing the resonant dual-tone operator $\hat{U}_{AB}$. We find that two different decompositions of arbitrary SU(3) gates using three SU(2) rotations result in comparable fidelities. The dual-tone operator $\hat{U}_{AB}$ is particularly useful for qutrit operations in platforms where one coupling is forbidden or inconvenient to use, not only in the ultracold atomic states used here, but also in systems such as superconducting qutrits [21] and ions [11]. In our experiments, for example, we reduced the number of steps required for tomography to single-step operations for $\hat{R}_5$ and $\hat{R}_6$.

When decomposing SU(d) operations into SU(2) steps, the number of operations scales quadratically with d. In the future, alternative approaches to SU(3) operations could be implemented by decomposing via Householder reflections rather than SU(2) operations, which scales linearly with d by applying dual-tone time-dependent pulses with detuning [29]. Additionally, optimization using quantum control techniques is promising for increasing the speed and fidelity of qutrit and qudit operations [47,48]. Refs. [30,31] have used phase-modulated signals for quantum control in ^{133}Cs using $d = 7$ and $d = 16$. Using two fully independent transitions A, B with their own modulations may lead to faster and more efficient optimized gates.

Looking forward, the two-qutrit operations necessary for universal quantum information processing [1,27,49] will expand the scope of these initial demonstrations, whether in ensembles [50] or single-atom arrays [34]. Opportunities in broader areas, such as for holonomic computing [20,51–54] will also take benefit from a comprehensive control over the multilevel state systems developed for qutrit and qudits. While there is increasing potential for neutral atoms to serve in these roles, the general techniques for quantum state control over qudits apply across platforms, and developments across fields will rapidly accelerate these capabilities for all systems.

APPENDIX A: OPERATOR DERIVATIONS

Here we provide details of the operators necessary for the SU(3) decompositions $\hat{U}^I$ and $\hat{U}^{II}$.

1. Coupling Operators

The coupling operators $\hat{U}_A$, $\hat{U}_B$, and $\hat{U}_{AB}$ are produced by driving resonant microwave couplings between states $\{|0\rangle, |1\rangle\}$ and $\{|1\rangle, |2\rangle\}$, as shown in Fig. 2(a). In general, when such a resonant dual-tone field is applied to a three-level system, the lab-frame Hamiltonian in the basis $\{|0\rangle, |1\rangle, |2\rangle\}^T$ is

$$\hat{H} = \hbar \begin{pmatrix} \omega_A & |\Omega_A| \sin(\omega_A t + \phi_A) & 0 \\ |\Omega_A| \sin(\omega_A t + \phi_A) & 0 & |\Omega_B| \sin(\omega_B t + \phi_B) \\ 0 & |\Omega_B| \sin(\omega_B t + \phi_B) & \omega_B \end{pmatrix}, \quad (A1)$$

where ω_X, ϕ_X and Ω_X are the resonant frequency, phase, and Rabi frequency for the transition $X \in \{A, B\}$ shown in Fig. 1. A useful rotating frame for this analysis is generated by the rotation

$$\hat{W} = \begin{pmatrix} e^{i\omega_A t} & 0 & 0 \\ 0 & 1 & 0 \\ 0 & 0 & e^{i\omega_B t} \end{pmatrix}. \quad (A2)$$

After transforming the Hamiltonian into this frame $\hat{\tilde{H}} = \hat{W}^\dagger \hat{H} \hat{W} + i\hbar (\partial_t \hat{W}) \hat{W}^\dagger$ and applying the rotating-wave approximation, the new effective Hamiltonian is

$$\hat{\tilde{H}} = \frac{i\hbar}{2} \begin{pmatrix} 0 & -\Omega_A & 0 \\ \Omega_A^* & 0 & \Omega_B^* \\ 0 & -\Omega_B & 0 \end{pmatrix}, \quad (A3)$$

where $\Omega_X = |\Omega_X| e^{i\phi_X}$ is the complex coupling parameter. A single-qutrit gate operation performed by applying this Hamiltonian for some duration t is

$$\hat{U} = \exp(-i\hat{\tilde{H}} t / \hbar). \quad (A4)$$

As one ingredient in our decomposition, we consider SU(2) coupling gates realized by applying a single-tone field. If, for example, we impose the condition $\Omega_B = 0$ on Eq. (A3) before using this Hamiltonian to calculate the evolution (A4) for some duration $t_A = 2\tau_A/|\Omega_A|$, we find a gate operating only on the $|0\rangle \leftrightarrow |1\rangle$ subspace

$$\hat{U}_A(\tau_A, \phi_A) = \begin{pmatrix} \cos \tau_A & -e^{i\phi_A} \sin \tau_A & 0 \\ e^{-i\phi_A} \sin \tau_A & \cos \tau_A & 0 \\ 0 & 0 & 1 \end{pmatrix}, \quad (A5)$$

which provides amplitude and phase control for the targeted coupling between $|0\rangle \leftrightarrow |1\rangle$. Similarly, for the condition $\Omega_A = 0$ and duration $t_B = 2\tau_B/|\Omega_B|$, we have

$$\hat{U}_B(\tau_B, \phi_B) = \begin{pmatrix} 1 & 0 & 0 \\ 0 & \cos \tau_B & e^{-i\phi_B} \sin \tau_B \\ 0 & -e^{i\phi_B} \sin \tau_B & \cos \tau_B \end{pmatrix} \quad (A6)$$

which achieves the same for the targeted coupling between $|1\rangle \leftrightarrow |2\rangle$.

To implement $\hat{U}_{AB}$, both coupling terms in (A3) are generally nonzero. If we restrict the pulse duration to $t_{AB} = 2\pi/\sqrt{|\Omega_A|^2 + |\Omega_B|^2}$ as was first explained in Ref. [11], we find the resonant dual-tone operator first shown in that paper,

$$\hat{U}_{AB}(\alpha, \beta) = \begin{pmatrix} \cos(\alpha) & 0 & -e^{i\beta} \sin(\alpha) \\ 0 & -1 & 0 \\ -e^{-i\beta} \sin(\alpha) & 0 & -\cos(\alpha) \end{pmatrix}, \quad (A7)$$

where to simplify the expression we have defined $\alpha = 2 \arctan |\Omega_A/\Omega_B|$ and $\beta = \arg(\Omega_A/\Omega_B)$. Under this condition for the operator time, the coupling is directly between the states $|0\rangle \leftrightarrow |2\rangle$.

In addition to the SU(2) couplings demonstrated here, a diagonal phase gate is required to span SU(3).

2. Virtual Phase Gates

While Ref. [11] suggests applying far-off resonance fields to perform the phase gate

$$\hat{U}_\theta(\eta, \varepsilon) = \exp \begin{pmatrix} i\eta & 0 & 0 \\ 0 & i\varepsilon & 0 \\ 0 & 0 & -i(\eta + \varepsilon) \end{pmatrix}, \qquad (A8)$$

recent qutrit experiments [21–24] have implemented diagonal phase gates virtually, by manipulating proceeding control fields rather than by manipulating the atoms directly. As they are adjustments to control fields, these virtual phase gates are efficient and have zero duration [55].

Any unitary operators $\hat{U}_a$ that are to be implemented after phase gate $\hat{U}_\theta$ are simply phase-shifted by the transformation

$$\hat{\tilde{U}}_a = \hat{U}_\theta^\dagger \hat{U}_a \hat{U}_\theta. \qquad (A9)$$

This effectively delays application of the $\hat{U}_\theta$ operator until the end of the pulse sequence—notice the location of $\hat{U}_\theta$ in the following operator sequence:

$$\begin{aligned} \hat{U}_{\text{gen.}} &= \hat{U}_{a_3} \hat{U}_{a_2} \hat{U}_{a_1} \hat{U}_\theta \hat{U}_b \\ &= \hat{U}_\theta \hat{U}_\theta^\dagger \hat{U}_{a_3} \hat{U}_\theta \hat{U}_\theta^\dagger \hat{U}_{a_2} \hat{U}_\theta \hat{U}_\theta^\dagger \hat{U}_{a_1} \hat{U}_\theta \hat{U}_b \\ &= \hat{U}_\theta \hat{\tilde{U}}_{a_3} \hat{\tilde{U}}_{a_2} \hat{\tilde{U}}_{a_1} \hat{U}_b. \end{aligned} \qquad (A10)$$

Several virtual phase gates are easily combined by tracking the accumulated η and ε through the operator sequence.

The remaining final $\hat{U}_\theta$ operator never needs to be applied because after the last coupling operator (including tomography pulses), the state is projected via $|\langle n| \hat{U}_{\text{gen.}} |\psi\rangle|^2$, and the phase information is destroyed.

In our experiment, the readout operators $\hat{R}_i$ are applied after the diagonal phase gate $\hat{U}_\theta$, so these pulses are phase shifted in practice, and modified pulses $\hat{\tilde{R}}_i$ are generated:

$$\hat{\tilde{R}}_{1,2}(\phi) = \hat{R}_{1,2}(\phi + \varepsilon - \eta), \qquad (A11)$$

$$\hat{\tilde{R}}_{3,4}(\phi) = \hat{R}_{3,4}(\phi - \eta - 2\varepsilon), \qquad (A12)$$

$$\hat{\tilde{R}}_{5,6}(\phi) = \hat{R}_{5,6}(\phi - \varepsilon - 2\eta). \qquad (A13)$$

3. Fourier Transform

The Fourier transform $\hat{F}$ does not have determinant 1, so it is not a member of the group SU(3); however, $i\hat{F}$ is in the group, so the operation can be achieved up to a global phase. The decomposition $\hat{F}^{\text{I}}$ differs from (1) by the change of basis $|1\rangle \leftrightarrow |2\rangle$, and the decomposition $\hat{F}^{\text{II}}$ differs from (1) by the change of basis $|0\rangle \leftrightarrow |1\rangle$.

TABLE IV. Parameters for Operator Decomposition.

Decomposition	Step, k	$\hat{U}_k$	a	Coupling basis $\{|m\rangle, |n\rangle\}$
$\hat{U}^{\text{I}} = \hat{U}_\theta \hat{U}_A \hat{U}_B \hat{U}_A$	1	$\hat{U}_{\text{gen.}}$	$|2\rangle$	A: $\{|0\rangle, |1\rangle\}$
	2	$\hat{U}_{\text{gen.}} \hat{U}_1^\dagger$	$|2\rangle$	B: $\{|1\rangle, |2\rangle\}$
	3	$\hat{U}_{\text{gen.}} \hat{U}_1^\dagger \hat{U}_2^\dagger$	$|1\rangle$	A: $\{|0\rangle, |1\rangle\}$
$\hat{U}^{\text{II}} = \hat{U}_\theta \hat{U}_A \hat{U}_B \hat{U}_{AB}$	1	$\hat{U}_{\text{gen.}}$	$|2\rangle$	AB: $\{|0\rangle, |2\rangle\}$
	2	$\hat{U}_{\text{gen.}} \hat{U}_1^\dagger$	$|2\rangle$	B: $\{|1\rangle, |2\rangle\}$
	3	$\hat{U}_{\text{gen.}} \hat{U}_1^\dagger \hat{U}_2^\dagger$	$|1\rangle$	A: $\{|0\rangle, |1\rangle\}$

4. Decomposition of Operators

The supplementary material of Ref. [22] shows an algorithm for decomposition of any arbitrary qutrit gate $\hat{U}_{\text{gen.}}$ into SU(2) steps using two single-tone couplings. We show a version of the procedure that works for either single- or dual-tone decompositions here for clarity and because we suspect that exposition has typographical errors. A SU(2) coupling on the basis $\{|m\rangle, |n\rangle\}$ of area τ and phase ϕ can be expressed as

$$R^{mn}(\tau, \phi) = \exp \left\{ -i\frac{\tau}{2} \left[\cos(\phi)\sigma_x^{mn} + \sin(\phi)\sigma_y^{mn} \right] \right\} \qquad (A14)$$

where $\sigma_x^{mn} = |m\rangle\langle n| + |n\rangle\langle m|$ and $\sigma_y^{mn} = i|n\rangle\langle m| - i|m\rangle\langle n|$. Each step of the rotation has

$$\tau = 2 \arcsin \sqrt{ \frac{|\langle a|\hat{U}_k|m\rangle|^2}{|\langle a|\hat{U}_k|m\rangle|^2 + |\langle a|\hat{U}_k|n\rangle|^2} } \qquad (A15)$$

and

$$\phi = \frac{\pi}{2} + \arg\left(\langle a|\hat{U}_k|m\rangle\right) - \arg\left(\langle a|\hat{U}_k|n\rangle\right), \qquad (A16)$$

where $\langle a|\hat{U}_k|m\rangle$ is a matrix element of $\hat{U}_k$ to be zeroed and $\hat{U}_k$ is the remaining portion of $\hat{U}_{\text{gen.}}$ to be implemented. The values of $|a\rangle$, $|m\rangle$, $|n\rangle$, and $\hat{U}_k$ to be used for each step of the decomposition are given in Table IV.

APPENDIX B: EXPERIMENTAL CONSIDERATIONS

1. Signal Generation

To generate microwave signals with arbitrary phase, frequency, and amplitude control, we mix the output of an arbitrary waveform generator with a microwave signal. The microwave signal is detuned 100 MHz below the hyperfine splitting of ^{87}Rb, and is produced by a BNC Model 845 microwave signal generator. A Tektronix AWG5204 controlled by PYTHON software produces signals at 5 GS/s which are preamplified before

being combined with the microwave-frequency signal in a double-balanced mixer. The mixed signal is amplified by a 25 W microwave amplifier before being directed towards the atoms through a waveguide. Higher Rabi frequencies would certainly be achievable with higher microwave power or a more focused beam.

2. Error Mechanisms

In this section we discuss and evaluate some mechanisms in our system that could cause the fidelity and purity errors from Table III in the main text. We note that dephasing is not a leading source of error, as our T_2^* times are well over 1 ms.

3. Detuning

When performing manipulations using our apparatus, we frequently find readjusting magnetic field biases necessary to keep the two generated frequencies resonant with the atomic frequencies ω_A and ω_B. This field instability of order 30 min is a limitation of our system, and not a limitation of neutral atom computation in general. Because of concerns about the continued resonance of operations, in addition to frequent checks of the biases we average final populations for tomographic tests as discussed in the main text.

We numerically simulate the operations $\hat{F}^{\mathrm{I}}$ and $\hat{F}^{\mathrm{II}}$, adding detuning deliberately,

$$\hat{H}_{\mathrm{detun.}} = \hbar \begin{pmatrix} \omega_A & |\Omega_A| \sin((\omega_A + \Delta_A)t + \phi_A) & 0 \\ |\Omega_A| \sin((\omega_A + \Delta_A)t + \phi_A) & 0 & |\Omega_B| \sin((\omega_B + \Delta_B)t + \phi_B) \\ 0 & |\Omega_B| \sin((\omega_B + \Delta_B)t + \phi_B) & \omega_B \end{pmatrix} \quad \text{(B1)}$$

$$\hat{\tilde{H}}_{\mathrm{detun.}} = \frac{i\hbar}{2} \begin{pmatrix} 0 & -\Omega_A e^{i\Delta_A t} & 0 \\ (\Omega_A e^{i\Delta_A t})^* & 0 & (\Omega_B e^{i\Delta_B t})^* \\ 0 & -\Omega_B e^{i\Delta_B t} & 0 \end{pmatrix}, \quad \text{(B2)}$$

and, setting $\Delta = \Delta_A = -\Delta_B$ for each of the decomposed SU(2) steps, generate the curves of Fig. 5. If detuning, applied equally to all atoms in the ensemble, was a strong error mechanism in our system, we would expect to see lower $\mathcal{F}$ for the dual-tone $\hat{F}^{\mathrm{II}}$ than the single-tone $\hat{F}^{\mathrm{I}}$, and we would not expect to see a drop in $\mathcal{P}$. In our experiment, the fidelity for both decompositions is of a similar magnitude, and we observe a significant drop in $\mathcal{P}$, so this

detuning model does not explain the main error mechanism present.

4. Stark Shifts Caused by the Optical Dipole Trap

During the application of microwave pulses for state manipulation, the atomic ensemble is held in a two-beam crossed optical dipole trap. This laser with approximately 0.4 W of power holds atoms in place by creating a three-dimensional Gaussian trap with depth 6 μK. The potential experienced by the Bose-Einstein condensed atoms near its center is approximated by a spherically symmetric harmonic oscillator with trap frequency $\omega_{\mathrm{ho}} \approx 2\pi \times 100$ Hz. The 10^5 atoms are held within a Thomas-Fermi radius $R_{\mathrm{TF}} = 6.5$ μm.

In a hyperfine manifold, we expect Stark shifts to take the form [56,57]

$$E_S = -\frac{1}{2}\alpha_0 \mathcal{E}^2 - \frac{1}{2}\alpha_2^F \mathcal{E}^2 \left[\frac{3m_F^2 - F(F+1)}{F(2F-1)} \right], \quad \text{(B3)}$$

where α_0 is the scalar polarizability of the ground state, α_2^F is the tensor polarizability for hyperfine level F, m_F is the Zeeman sublevel, and $\mathcal{E}$ is the electric field strength.

The scalar Stark shift will perturb the energy of both the $|F = 1\rangle$ manifold and the $|F = 2\rangle$ manifold equally. As a result, regardless of the position of the atoms in the trap, all atoms will simultaneously be resonant. At the center of the
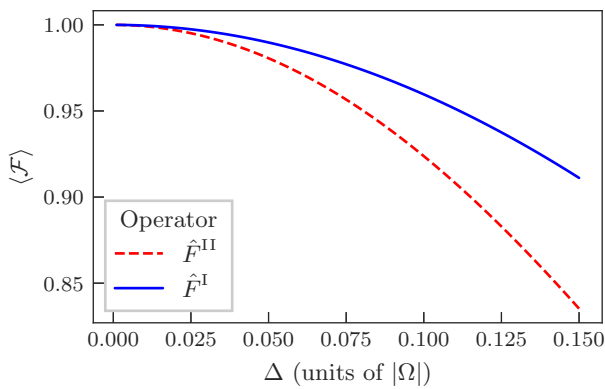

FIG. 5.   Simulated effect of detuning on the final fidelity measurement, averaged across the states $|0\rangle$, $|1\rangle$, and $|2\rangle$, where $\Omega^2 = |\Omega_A|^2 + |\Omega_B|^2$.

cloud, both levels are shifted by about $h \times 6.0$ kHz. At R_{TF} from the center, the shift is about $h \times 5.9$ kHz, a difference of about $h \times 100$ Hz.

The tensor Stark shift perturbs the energy of the $|F = 1, m_F = 1\rangle = |1\rangle$ state without having an effect on $|F = 2\rangle$ states. As a result, atoms in the center of the trap will have different resonant frequencies for both transitions ω_A and ω_B from atoms at the two ends of the trap. The magnitude of the tensor shift for $|1\rangle$ is $h \times 25.8$ kHz at the center of the trap and $h \times 25.3$ kHz at R_{TF}. The probability distribution function is [58]

$$
\begin{aligned}
n_{1\text{D}}(r) &= \int_{4\pi} r^2 d\Omega \, n_{3D}(\mathbf{r}) \\
&= \int_{4\pi} r^2 d\Omega \frac{\mu}{g} \left(1 - \frac{r^2}{R_{\text{TF}}^2} \right) \\
&= \frac{4\pi \mu r^2}{g} \left(1 - \frac{r^2}{R_{\text{TF}}^2} \right),
\end{aligned}
\tag{B4}
$$

where r is the radial coordinate, m_{Rb} is the mass of an ^{87}Rb atom, $\mu = m_{\text{Rb}}\omega_{\text{ho}}^2 R_{\text{TF}}^2/2$ is the chemical potential, and $g = 4\pi \hbar^2 a/m_{\text{Rb}}$ is the coupling constant. 1D denotes one dimensional. We can obtain the mean Stark shift,

$$
\langle E_S \rangle = \int dr \, n_{1\text{D}}(r) E_S(r),
\tag{B5}
$$

and assuming our frequency calibration is accurate to this mean, the detuning,

$$
\Delta(r) = E_S(r) - \langle E_S \rangle.
\tag{B6}
$$

To evaluate the purity and fidelity decay caused by the tensor Stark shift, we sample 1000 detunings from $\Delta(r)$, weight them by $n_{1\text{D}}(r)$, and calculate the $\hat{\rho}_{\text{out}}$ found by tomography from this distribution comparing it to the $\hat{\rho}$ for Stark-shift-free evolution. The results are shown in Table V.

Finally, we performed these experiments in a trap to mimic the environment of a practical quantum processor based on neutral atoms, which would require some trapping potential to maintain the atoms in position throughout an extended computation. However, measurements like the

ones made in this work could be performed in time of flight (as other demonstrations have done) to avoid Stark shifts.

We also perform the same purity recovery algorithm from (5), with results shown in Table V. As expected, the purity recovery algorithm results in a perfect fidelity. We conclude that it is plausible that the relatively low purity and some of the error in $\mathcal{F}$ we find in the main results (Table III) may be caused by Stark shifts from the optical dipole trap.

5. Calibration

For a high-fidelity operator, the many control pulses used in our experiment including $\hat{U}_{\text{prep.}}$, $\hat{U}_A$, $\hat{U}_B$, $\hat{U}_{AB}$, and $\hat{R}_i$ must simultaneously have their pulse durations calibrated accurately and the detuning for both tones must be negligible (less than $0.025|\Omega| \approx 2\pi \times 50$ Hz as suggested by Fig. 5).

To find the resonant frequencies, the duration and frequency of the two tones were adjusted manually until 100 % of the atomic population was transferred between the states. The duration of each operator was also calibrated manually by starting from each computational basis state and scanning the operator duration to find the point where the population transfer matches theory.

In the ideal case, we would assume Ω is constant during the application of an operator, and we could determine the Rabi frequency to high precision by performing long pulses $\tau = n\pi$. In our system, long pulses would not be a good calibration technique because the Rabi frequency Ω is not constant over longer time periods. This may be a limitation of our microwave amplifier or magnetic field bias stability. To account for this effect, each pulse duration was calibrated individually for its position in the pulse sequence, and only short pulses were used in the experiment.

Our current microwave system is not optimized for high Rabi frequencies. A rectangular waveguide is aimed towards the atoms from a distance of approximately 15 cm before the microwaves are allowed to propagate through free space. The microwaves which impinge on the atoms are sent off-axis and do not demonstrate any significant degree of polarization, driving σ^+, σ^-, and π transitions. Work is under way to improve this system significantly by using a helical antenna to generate well-defined $\sigma^\pm$ polarizations based on the work of Ref. [59].

TABLE V. Simulated reduction in fidelity, purity, and purity-adjusted fidelity due to trap-induced Stark shifts.

Operator	State	$\mathcal{P}$	$\mathcal{F}$	$\mathcal{F}_{\text{pure}}$
$\hat{F}^{\text{II}}$	$|0\rangle$	0.953	0.980	1.009
	$|1\rangle$	0.950	0.974	1.008
	$|2\rangle$	0.953	0.980	1.009
$\hat{F}^{\text{I}}$	$|0\rangle$	0.963	0.981	1.006
	$|1\rangle$	0.965	0.986	1.007
	$|2\rangle$	0.965	0.986	1.007

[1] Y. Wang, Z. Hu, B. C. Sanders, and S. Kais, Qudits and high-dimensional quantum computing, Front. Phys. **8**, 589504 (2020).

[2] C. M. Caves and G. J. Milburn, Qutrit entanglement, Opt. Commun. **179**, 439 (2000).

[3] S. Dogra, Arvind, and K. Dorai, Determining the parity of a permutation using an experimental NMR qutrit, Phys. Lett. A **378,** 3452 (2014).

[4] Z. Gedik, I. A. Silva, B. Çakmak, G. Karpat, E. L. Vidoto, D. O. Soares-Pinto, E. R. DeAzevedo, and F. F. Fanchini, Computational speed-up with a single qudit, Sci. Rep. **5,** 14671 (2015).

[5] D. Bruß and C. Macchiavello, Optimal Eavesdropping in Cryptography with Three-Dimensional Quantum States, Phys. Rev. Lett. **88,** 127901 (2002).

[6] G. Molina-Terriza, A. Vaziri, R. Ursin, and A. Zeilinger, Experimental Quantum Coin Tossing, Phys. Rev. Lett. **94,** 040501 (2005).

[7] S. S. Ivanov, H. S. Tonchev, and N. V. Vitanov, Time-efficient implementation of quantum search with qudits, Phys. Rev. A **85,** 062321 (2012).

[8] B. P. Lanyon, M. Barbieri, M. P. Almeida, T. Jennewein, T. C. Ralph, K. J. Resch, G. J. Pryde, J. L. O'Brien, A. Gilchrist, and A. G. White, Simplifying quantum logic using higher-dimensional Hilbert spaces, Nat. Phys. **5,** 134 (2009).

[9] A. Bocharov, M. Roetteler, and K. M. Svore, Factoring with qutrits: Shor's algorithm on ternary and metaplectic quantum architectures, Phys. Rev. A **96,** 012306 (2017).

[10] P. Gokhale, J. M. Baker, C. Duckering, F. T. Chong, N. C. Brown, and K. R. Brown, Extending the frontier of quantum computers with qutrits, IEEE Micro **40,** 64 (2020).

[11] A. B. Klimov, R. Guzmán, J. C. Retamal, and C. Saavedra, Qutrit quantum computer with trapped ions, Phys. Rev. A **67,** 7 (2003).

[12] D. Mc Hugh and J. Twamley, Trapped-ion qutrit spin molecule quantum computer, New J. Phys. **7,** 174 (2005).

[13] Y. I. Bogdanov, M. V. Chekhova, S. P. Kulik, G. A. Maslennikov, A. A. Zhukov., C. H. Oh, and M. K. Tey, Qutrit State Engineering with Biphotons, Phys. Rev. Lett. **93,** 230503 (2004).

[14] S. Gröblacher, T. Jennewein, A. Vaziri, G. Weihs, and A. Zeilinger, Experimental quantum cryptography with qutrits, New J. Phys. **8,** 75 (2006).

[15] B. P. Lanyon, T. J. Weinhold, N. K. Langford, J. L. O'Brien, K. J. Resch, A. Gilchrist, and A. G. White, Manipulating Biphotonic Qutrits, Phys. Rev. Lett. **100,** 060504 (2008).

[16] C. Schaeff, R. Polster, M. Huber, S. Ramelow, and A. Zeilinger, Experimental access to higher-dimensional entangled quantum systems using integrated optics, Optica **2,** 523 (2015).

[17] A. Babazadeh, M. Erhard, F. Wang, M. Malik, R. Nouroozi, M. Krenn, and A. Zeilinger, High-Dimensional Single-Photon Quantum Gates: Concepts and Experiments, Phys. Rev. Lett. **119,** 180510 (2017).

[18] H. Lu, Z. Hu, M. S. Alshaykh, A. J. Moore, Y. Wang, P. Imany, A. M. Weiner, and S. Kais, Quantum phase estimation with time-frequency qudits in a single photon, Adv. Quantum Technol. **3,** 1900074 (2020).

[19] R. Bianchetti, S. Filipp, M. Baur, J. M. Fink, C. Lang, L. Steffen, M. Boissonneault, A. Blais, and A. Wallraff, Control and Tomography of a Three Level Superconducting Artificial Atom, Phys. Rev. Lett. **105,** 223601 (2010).

[20] S. Danilin, A. Vepsäläinen, and G. S. Paraoanu, Experimental state control by fast non-Abelian holonomic gates with a superconducting qutrit, Phys. Scr. **93,** 055101 (2018).

[21] M. A. Yurtalan, J. Shi, M. Kononenko, A. Lupascu, and S. Ashhab, Implementation of a Walsh-Hadamard Gate in a Superconducting Qutrit, Phys. Rev. Lett. **125,** 180504 (2020).

[22] M. Kononenko, M. A. Yurtalan, S. Ren, J. Shi, S. Ashhab, and A. Lupascu, Characterization of control in a superconducting qutrit using randomized benchmarking, Phys. Rev. Res. **3,** L1042007 (2021).

[23] M. S. Blok, V. V. Ramasesh, T. Schuster, K. O'Brien, J. M. Kreikebaum, D. Dahlen, A. Morvan, B. Yoshida, N. Y. Yao, and I. Siddiqi, Quantum Information Scrambling on a Superconducting Qutrit Processor, Phys. Rev. X **11,** 21010 (2021).

[24] A. Morvan, V. V. Ramasesh, M. S. Blok, J. M. Kreikebaum, K. O'Brien, L. Chen, B. K. Mitchell, R. K. Naik, D. I. Santiago, and I. Siddiqi, Qutrit Randomized Benchmarking, Phys. Rev. Lett. **126,** 210504 (2021).

[25] J. Randall, S. Weidt, E. D. Standing, K. Lake, S. C. Webster, D. F. Murgia, T. Navickas, K. Roth, and W. K. Hensinger, Efficient preparation and detection of microwave dressed-state qubits and qutrits with trapped ions, Phys. Rev. A **91,** 012322 (2015).

[26] T. Bækkegaard, L. B. Kristensen, N. J. S. Loft, C. K. Andersen, D. Petrosyan, and N. T. Zinner, Realization of efficient quantum gates with a superconducting qubit-qutrit circuit, Sci. Rep. **9,** 13389 (2019).

[27] P. J. Low, B. M. White, A. A. Cox, M. L. Day, and C. Senko, Practical trapped-ion protocols for universal qudit-based quantum computing, Phys. Rev. Res. **2,** 033128 (2020).

[28] M. Ringbauer, M. Meth, L. Postler, R. Stricker, R. Blatt, P. Schindler, and T. Monz, A universal qudit quantum processor with trapped ions, Nat. Phys. **18,** 1053 (2022).

[29] N. V. Vitanov, Synthesis of arbitrary SU(3) transformations of atomic qutrits, Phys. Rev. A **85,** 032331 (2012).

[30] S. Chaudhury, S. Merkel, T. Herr, A. Silberfarb, I. H. Deutsch, and P. S. Jessen, Quantum Control of the Hyperfine Spin of a Cs Atom Ensemble, Phys. Rev. Lett. **99,** 163002 (2007).

[31] B. E. Anderson, H. Sosa-Martinez, C. A. Riofrío, I. H. Deutsch, and P. S. Jessen, Accurate and Robust Unitary Transformations of a High-Dimensional Quantum System, Phys. Rev. Lett. **114,** 240401 (2015).

[32] M. Saffman, Quantum computing with atomic qubits and Rydberg interactions: Progress and challenges, J. Phys. B **49,** 202001 (2016).

[33] S. Olmschenk, R. Chicireanu, K. D. Nelson, and J. V. Porto, Randomized benchmarking of atomic qubits in an optical lattice, New J. Phys. **12,** 113007 (2010).

[34] L. Henriet, L. Beguin, A. Signoles, T. Lahaye, A. Browaeys, G.-O. Reymond, and C. Jurczak, Quantum computing with neutral atoms, Quantum **4,** 327 (2020).

[35] D. Bluvstein, H. Levine, G. Semeghini, T. T. Wang, S. Ebadi, M. Kalinowski, A. Keesling, N. Maskara, H. Pichler, M. Greiner, V. Vuletić, and M. D. Lukin, A quantum processor based on coherent transport of entangled atom arrays, Nature **604,** 451 (2022).

[36] Y. Wang, X. Zhang, T. A. Corcovilos, A. Kumar, and D. S. Weiss, Coherent Addressing of Individual Neutral Atoms in a 3D Optical Lattice, Phys. Rev. Lett. **115,** 043003 (2015).

[37] Y. Wang, A. Kumar, T.-Y. Wu, and D. S. Weiss, Single-qubit gates based on targeted phase shifts in a 3D neutral atom array, Science **352,** 1562 (2016).

[38] Y. Wang, S. Crain, C. Fang, B. Zhang, S. Huang, Q. Liang, P. H. Leung, K. R. Brown, and J. Kim, High-Fidelity Two-Qubit Gates Using a Microelectromechanical-System-Based Beam Steering System for Individual Qubit Addressing, Phys. Rev. Lett. **125,** 150505 (2020).

[39] L.-M. Steinert, P. Osterholz, R. Eberhard, L. Festa, N. Lorenz, Z. Chen, A. Trautmann, and C. Gross, Spatially programmable spin interactions in neutral atom arrays, arXiv.org , arXiv:2206.12385 (2022).

[40] V. Novičenko and G. Juzeliūnas, Non-Abelian geometric phases in periodically driven systems, Phys. Rev. A **100,** 012127 (2019).

[41] Z. Chen, J. D. Murphree, and N. P. Bigelow, SU(2) geometric phase induced by a periodically driven Raman process in an ultracold dilute Bose gas, Phys. Rev. A **101,** 013606 (2020).

[42] S. Sugawa, F. Salces-Carcoba, Y. Yue, A. Putra, and I. B. Spielman, Wilson loop and Wilczek-Zee phase from a non-Abelian gauge field, npj Quantum Inf. **7,** 144 (2021).

[43] A. I. Lvovsky, Iterative maximum-likelihood reconstruction in quantum homodyne tomography, J. Opt. B **6,** S565 (2004).

[44] R. Jozsa, Fidelity for mixed quantum states, J. Mod. Opt. **41,** 2315 (1994).

[45] D. D. Yavuz, P. B. Kulatunga, E. Urban, T. A. Johnson, N. Proite, T. Henage, T. G. Walker, and M. Saffman, Fast ground State Manipulation of Neutral Atoms in Microscopic Optical Traps, Phys. Rev. Lett. **96,** 063001 (2006).

[46] M. P. A. Jones, J. Beugnon, A. Gaëtan, J. Zhang, G. Messin, A. Browaeys, and P. Grangier, Fast quantum state control of a single trapped neutral atom, Phys. Rev. A **75,** 040301 (2007).

[47] J. Randall, A. M. Lawrence, S. C. Webster, S. Weidt, N. V. Vitanov, and W. K. Hensinger, Generation of high-fidelity quantum control methods for multilevel systems, Phys. Rev. A **98,** 043414 (2018).

[48] S. Omanakuttan, A. Mitra, M. J. Martin, and I. H. Deutsch, Quantum optimal control of ten-level nuclear spin qudits in ^{87}Sr, Phys. Rev. A **104,** L060401 (2021).

[49] M. Luo and X. Wang, Universal quantum computation with qudits, Sci. China Phys., Mech. Astron. **57,** 1712 (2014).

[50] M. Ebert, M. Kwon, T. G. Walker, and M. Saffman, Coherence and Rydberg Blockade of Atomic Ensemble Qubits, Phys. Rev. Lett. **115,** 093601 (2015).

[51] P. Zanardi and M. Rasetti, Holonomic quantum computation, Phys. Lett. A **264,** 94 (1999).

[52] G. Feng, G. Xu, and G. Long, Experimental Realization of Nonadiabatic Holonomic Quantum Computation, Phys. Rev. Lett. **110,** 190501 (2013).

[53] B. B. Zhou, P. C. Jerger, V. O. Shkolnikov, F. J. Heremans, G. Burkard, and D. D. Awschalom, Holonomic Quantum Control by Coherent Optical Excitation in Diamond, Phys. Rev. Lett. **119,** 140503 (2017).

[54] Y. Xu, Z. Hua, T. Chen, X. Pan, X. Li, J. Han, W. Cai, Y. Ma, H. Wang, Y. P. Song, Z.-Y. Xue, and L. Sun, Experimental Implementation of Universal Nonadiabatic Geometric Quantum Gates in a Superconducting Circuit, Phys. Rev. Lett. **124,** 230503 (2020).

[55] D. C. McKay, C. J. Wood, S. Sheldon, J. M. Chow, and J. M. Gambetta, Efficient Z gates for quantum computing, Phys. Rev. A **96,** 022330 (2017).

[56] M. Auzinsh, D. Budker, and S. Rochester, *Optically Polarized Atoms* (Oxford University Press, Oxford, 2010).

[57] D. A. Steck, *Rubidium 87 D Line Data*, Tech. Rep. 2 (Author, 2010).

[58] F. Dalfovo, S. Giorgini, L. P. Pitaevskii, and S. Stringari, Theory of Bose-Einstein condensation in trapped gases, Rev. Mod. Phys. **71,** 463 (1999).

[59] Y.-G. Zheng, L. Jiang, Z.-H. Zhu, W.-Y. Zhang, Z.-Y. Zhou, B. Xiao, and Z.-S. Yuan, A compact gain-enhanced microwave helical antenna for ^{87}Rb atomic experiments, Rev. Sci. Instrum. **93,** 064701 (2022).